

A scaling analysis of transient natural convection in a reservoir model induced by iso-flux heating

Peng Yu^{1,†}, John C. Patterson¹ and Chengwang Lei¹

¹School of Civil Engineering, University of Sydney, Sydney, NSW 2006, Australia

(Received 21 March 2014; revised 6 October 2014; accepted 28 November 2014;
first published online 23 December 2014)

This study presents a detailed scaling analysis quantifying the transient behaviour of natural convection in a reservoir model induced by iso-flux surface heating. It is found that horizontal conduction, which has often been neglected in previous analyses, plays an important role in the development of the flow. Depending on the Rayleigh number, three possible pathways through which the flow develops towards the final steady state are identified. A thermal boundary layer initially grows downwards from the surface. When the thermal boundary layer reaches the sloping bottom and becomes indistinct, a horizontal temperature gradient establishes due to the increasing water depth in the offshore direction. A flow is then driven towards the offshore direction by a buoyancy-induced horizontal pressure gradient, which convects away the heat input from the water surface. On the other hand, the horizontal temperature gradient also conducts heat away. The flow behaviour is determined by the interaction between the horizontal conduction and convection. An interesting flow feature revealed by the present scaling analysis is that the region across which the thermal boundary layer encompasses the full water depth shrinks over time at a certain stage of the flow development. The shrinking process eventually stops when this region coincides with a conduction-dominated subregion. The present scaling results are verified by corresponding numerical simulations.

Key words: buoyant boundary layers, convection in cavities, gravity currents

1. Introduction

The underlying mechanisms that govern natural convection in lakes and reservoirs are of great significance in the successful management of these resources, particularly in terms of nutrient and pollutant transport. The nearshore bathymetry of an increasing water depth in the offshore direction of lakes and reservoirs implies that, as a result of approximately uniform heat fluxes at the surface during day-time heating and night-time cooling, the shallow region heats up or cools down more rapidly than the deeper region, setting up a horizontal temperature gradient, which drives a convective flow. This flow exchanges nutrients and pollutants between the nearshore and the central regions, and thus influences the water quality. There have been a

[†]Present address: Institute of High Performance Computing, Agency for Science, Technology and Research (A*STAR), Republic of Singapore. Email address for correspondence:

yup@ihpc.a-star.edu.sg

considerably large number of investigations on natural convection in nearshore lake waters, reservoir sidearms (the nearshore embayments connected to the main water body) or other shallow-water bodies with a sloping bottom, by using analytical, experimental and numerical methods (e.g. Adams & Wells 1984; Lei & Patterson 2002a; Farrow 2004).

The field study of Monismith, Imberger & Morison (1990) has demonstrated a clear picture of this thermally driven flow, which greatly enhanced the rate of horizontal exchange between the sidearm and the main body of the reservoir. Many pollutants in reservoir systems are shore-based, and this mechanism can therefore provide significant transport of these materials from the nearshore region to the central part. The recent field experiment of Monismith *et al.* (2006) indicates that the thermally driven flow may also be a generic feature of the hydrodynamics of coral reefs and coastal oceans in general. It also helps to alleviate the stress of coral bleaching and enhance connectivity between the reef and the ocean (Monismith 2007). The implications of this for coral reef health are clear, and the connection to a much wider tourism industry is apparent.

Experimental and numerical studies of natural convection in a simplified reservoir model have been performed by many researchers (e.g. Horsch & Stefan 1988; Horsch, Stefan & Gavali 1994; Lei & Patterson 2003; Bednarz, Lei & Patterson 2008). Horsch & Stefan (1988) and Horsch *et al.* (1994) investigated numerically and experimentally natural convection in a triangular enclosure with a constant heat flux at the surface. The transient behaviour of the flow with surface cooling including the formation of sinking thermals and the establishment of a full cavity-scale circulation was illustrated. Lei & Patterson (2002a) investigated natural convection in a triangular enclosure subject to solar radiation. Their results revealed that the flow development from an isothermal and stationary state passes through three distinct stages, namely, an initial stage dominated by bottom heating due to the absorption of penetrative radiation there, a transitional stage characterized by the onset of convective instability in the form of rising plumes, and a steady stage evidenced by a steady large-scale circulation across the sidearm. It is worth mentioning that most of the studies considered two-dimensional triangular enclosures. Moreover, Lei & Patterson (2003) showed that the two-dimensional simulation reproduces all of the flow features observed in a three-dimensional simulation.

In addition to the numerical and experimental studies, attempts have also been made to quantify the strength of the thermally driven flow by analytical methods. For natural convection above the sloping bottom in a stratified ocean, Phillips (1970) and Wunsch (1970) described a mechanism that drives the flow. The approximately adiabatic condition on the sloping bottom means that the horizontal isothermals in the stratified water body must curl over to become perpendicular to the sloping bottom, which creates an additional boundary layer there. A horizontal temperature gradient is then established, which in turn drives a flow down the slope. Based on this mechanism, Wunsch (1970) provided a scale for the thickness of the bottom layer in a stably stratified fluid. Horsch & Stefan (1988) presented a scale for the flow rate, which is approximately proportional to $Ra_c^{1/n}$, where Ra_c is the Rayleigh number over the range $10^4 < Ra_c < 10^8$ and $2 < n < 3$. Note that a laminar model is adopted in their study, and Ra_c is defined as $Ra_c = g\beta I_s h^4 / k\alpha\nu$, where g is the acceleration due to gravity, β is the thermal expansion coefficient, I_s is the surface heat flux, h is the maximum depth of the enclosure, k is the thermal conductivity, α is the thermal diffusivity and ν is the kinematic viscosity. However, they did not report detailed analysis with respect to this scale. Sturman, Oldham & Ivey (1999) developed a

set of scaling arguments to characterize the flow induced by surface cooling. The results were used to explain both field and experimental data, as well as published data from the literature. Based on a detailed scaling analysis, Lei & Patterson (2005) demonstrated that the unequal heat loss associated with the varying water depth is more prevailing than the Philips mechanism. They classified the flow into three regimes, namely conductive, transitional and convective regimes. More recently, Mao, Lei & Patterson (2010) introduced a variable offshore length scale to extend the scaling of Lei & Patterson (2005). Two different sets of scaling incorporating the offshore-distance dependence have been derived for the conduction-dominated region and stable-convection-dominated region, respectively, which are confirmed by their numerical simulations.

Based on a small-slope assumption, a zero-order asymptotic solution has been derived by Farrow & Patterson (1994) to quantify the circulation induced by absorption of radiation in a sidearm. Using scaling analysis, Lei & Patterson (2002*b*) found that the flow can also be classified broadly into conductive, transitional or convective regimes determined merely by the Rayleigh number. By adopting a variable length scale in the scaling analysis and including the exponential terms arising from the depth-dependent absorption of solar radiation and the heat flux due to the re-emission of residual radiation arriving at the sloping bottom, Mao, Lei & Patterson (2009) have demonstrated that the flow quantities depend on the horizontal position. They developed a set of scales (e.g. temperature, velocity, time, thermal boundary layer thickness, etc.) to describe the flow development across the water body, and revealed more detailed features of the flow, i.e. the entire flow domain may be separated into different subregions with distinct flow and thermal features.

Despite our understanding of natural convection in reservoir nearshore regions advancing significantly in recent years, it is still far from complete, particularly with respect to the transient behaviour of the flow. More specifically, the recent studies of Yu, Lei & Patterson (2012*a,b*) showed deviations of their simulations from the scaling predictions of Mao *et al.* (2010) in terms of the transient flow development in the reservoir model induced by surface flux. For example, the developing time for the flow to reach the quasi-steady state is much longer than that predicted by Mao *et al.* (2010); the velocity in the convection-dominated region decreases with the offshore distance instead of increasing monotonically with the offshore distance as predicted by Mao *et al.* (2010); and the flow in the whole convection-dominated region reaches the quasi-steady state at the same time instead of sequentially in the offshore direction as predicted by Mao *et al.* (2010). This has motivated the present analysis, which will reveal the detailed transient behaviour of natural convection in a reservoir nearshore region with a constant heating flux at the water surface. The thermal forcing condition considered here may represent the day-time heating case in cloudy weather. The present investigation includes a detailed scaling analysis as well as a comprehensive set of numerical simulations. The simulations serve to verify the scaling analysis and provide additional insight for understanding the mechanisms that drive the flow.

The organization of the rest of the paper is as follows. Section 2 describes the governing equations and boundary conditions. Section 3 provides a detailed scaling analysis to quantify the transient behaviour of the flow. The numerical techniques as well as a grid independence study are given in §4, followed by verification of the scaling analysis using the numerical results in §5. Finally, §6 draws some conclusions.

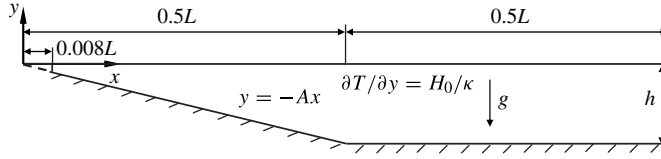


FIGURE 1. Schematic of the reservoir model. The symbol L denotes the total length of the reservoir. A very small tip region ($x < 0.008L$) is cut off to avoid singularity at the tip.

2. Model formulation

The reservoir model under consideration consists of a sloping-bottom region and an adjacent flat-bottom region. We perform the scaling analysis only for the sloping-bottom region as that adopted by Mao *et al.* (2009, 2010) because the sloping region provides the driving force for the convective flow in the reservoir. However, the flat region affects the scaling analysis in that it introduces a maximum water depth in the reservoir. The slope inclination is A ($A \ll 1$) and the maximum water depth is h . The reservoir is filled with water. A Cartesian coordinate system (x, y) is adopted, with the origin located at the tip of the reservoir model (refer to figure 1). The Navier–Stokes and energy equations governing the flow and temperature evolution are expressed as follows, in which the usual Boussinesq assumption has been made:

$$u_x + v_y = 0, \tag{2.1}$$

$$u_t + uu_x + vv_y = -\rho_0^{-1}p_x + \nu \nabla^2 u, \tag{2.2}$$

$$v_t + uv_x + vv_y = -\rho_0^{-1}p_y + \nu \nabla^2 v + g\beta(T - T_0), \tag{2.3}$$

$$T_t + uT_x + vT_y = \kappa \nabla^2 T. \tag{2.4}$$

Here u and v are the velocity components in the horizontal and vertical directions, respectively; x and y are the horizontal and vertical coordinates originating from the tip of the sloping region; t is time; T is the fluid temperature; and p is the pressure. The parameters ρ_0 , κ , ν and β are, respectively, the density, thermal diffusivity, kinematic viscosity and thermal expansion coefficient of water at a reference temperature T_0 (see below). Here, g is the acceleration due to gravity, which is in the negative y direction.

Initially ($t \leq 0$), the water in the reservoir is at rest and isothermal, that is,

$$u = v = 0, \tag{2.5}$$

$$T = T_0. \tag{2.6}$$

The water surface ($y = 0$) is assumed to be flat and stress-free, therefore

$$u_y = 0, \quad v = 0. \tag{2.7a,b}$$

The sloping and flat bottoms are rigid, no-slip and adiabatic. At the deep end, an open boundary condition is imposed, which is given by $\partial^2 u / \partial x^2 = \partial^2 v / \partial x^2 = \partial^2 T / \partial x^2 = 0$ and $\partial u / \partial x = \partial v / \partial x = \partial T / \partial x = 0$. Heating is introduced with a constant heat flux through the water surface as

$$T_y = \frac{1}{\kappa} \left(\frac{I_0}{\rho_0 C_p} \right) = \frac{H_0}{\kappa}, \quad y = 0, \quad t > 0, \tag{2.8}$$

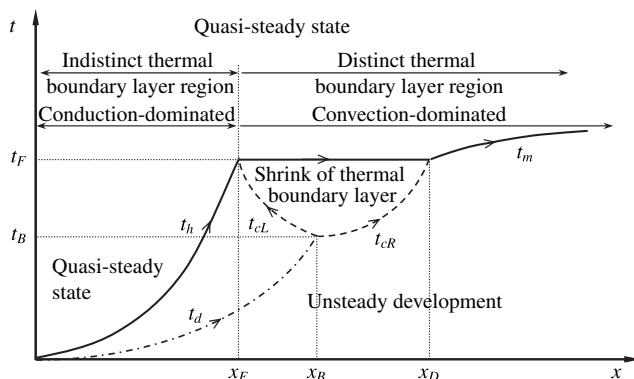


FIGURE 2. Schematic of possible flow development pathways towards the final quasi-steady state. The horizontal axis denotes the distance from the tip for the slope region. Here t_d is the time scale for the thermal boundary layer to reach the sloping bottom; t_h is the time scale to reach the quasi-steady state in the conduction-dominated subregion; t_{cL} and t_{cR} are the time scales at which the convection balance is achieved; and t_m is the time scale for the discharge flow.

where I_0 is the imposed surface heat flux, C_p is the specific heat of water at T_0 , and $H_0 = I_0/(\rho_0 C_p)$ is the volumetric heating intensity at the surface.

3. Scaling analysis

3.1. Overview of the flow development

In this section, the key scaling results are summarized to provide an overview of the flow development. When the water in the present reservoir model is exposed to a constant heat flux from the water surface for a sufficiently long time, the flow in the reservoir eventually reaches a quasi-steady state, in which temperature gradient and flow velocity become steady everywhere in the water body. The possible pathways through which the flow develops towards the final quasi-steady state, which depend on the Rayleigh number, are summarized in table 1. A schematic of the development pathways is shown in figure 2, and a schematic of the movements of the interfaces between the different subregions shown in figure 2 is given in figure 3.

Upon the initiation of the heat flux at the water surface, the thermal boundary layer initially grows downwards. Once the thermal boundary layer reaches the bottom, it becomes indistinct over the local water depth. When that happens, the thermal boundary layer is referred to as an indistinct thermal boundary layer. In contrast, a thermal boundary layer with thickness less than the full local water depth is referred to as a distinct thermal boundary layer. A horizontal temperature gradient develops in the indistinct thermal boundary layer region due to the variation of the water depth, which results in unequal heat gain over the local depth. A horizontal pressure gradient is then induced by buoyancy, which drives a horizontal flow in the offshore direction along the surface.

The flow is weak initially and conduction is dominant in the whole reservoir. The indistinct thermal boundary layer region expands in the offshore region (the dashed line x_d in figure 3a). Within the indistinct thermal boundary layer region, a conduction-dominated subregion develops and also expands in the offshore direction (the dashed line x_h in figure 3a). Within the conduction-dominated subregion, the

<i>Ra</i> range		Flow description
<i>Ra</i> < 1	$0 < t < h^2\kappa^{-1}$	The thermal boundary layer grows and attaches to the sloping bottom; initiation of a flow and the flow velocity increases with time.
	$t = h^2\kappa^{-1}$	The thermal boundary layer attaches to the bottom in the whole reservoir.
	$h^2\kappa^{-1} < t < \frac{1}{2}h^2A^{-2}\kappa^{-1}$	The horizontal temperature gradient and the flow velocity outside the conduction-dominated subregion increase with time.
	$t = \frac{1}{2}h^2A^{-2}\kappa^{-1}$	Flow reaches the quasi-steady state.
$1 < Ra < Ra_i$	$0 < t < h^2\kappa^{-1}$	The thermal boundary layer grows and attaches to the sloping bottom; initiation of a flow and the flow velocity increases with time.
	$t = h^2\kappa^{-1}$	The thermal boundary layer attaches to the bottom in the whole reservoir.
	$h^2\kappa^{-1} < t < t_B$	The horizontal temperature gradient and flow velocity outside of the conduction-dominated subregion keep increasing with time.
	$t = t_B$	The region with indistinct thermal boundary layer stops extending at $x = x_B$.
	$t_B < t < t_F$	The thermal boundary layer becomes distinct near the region with the maximum depth and convection becomes dominant there; the indistinct boundary layer region shrinks while the convection-dominated subregion expands; the flow velocity outside the conduction-dominated subregion increases with time.
	$t = t_F$	Flow reaches the quasi-steady state; the whole reservoir can be divided into conduction-dominated and convection-dominated subregions.
<i>Ra</i> > <i>Ra_i</i>	$0 < t < t_B$	The thermal boundary layer grows and attaches to the sloping bottom; initiation of a flow and the flow velocity increases with time.
	$t = t_B$	The indistinct thermal boundary layer region stops extending at $x = x_B$.
	$t_B < t < t_F$	Convection becomes dominant near the region around $x = x_B$; the indistinct boundary layer region shrinks and the convection-dominated subregion expands; the flow velocity outside the conduction-dominated subregion increases with time.
	$t = t_F$	Flow reaches the quasi-steady state; the whole reservoir can be divided into conduction-dominated and convection-dominated subregions; the convection-dominated subregion can be further divided into two subregions.

TABLE 1. Possible development pathways of the flow.

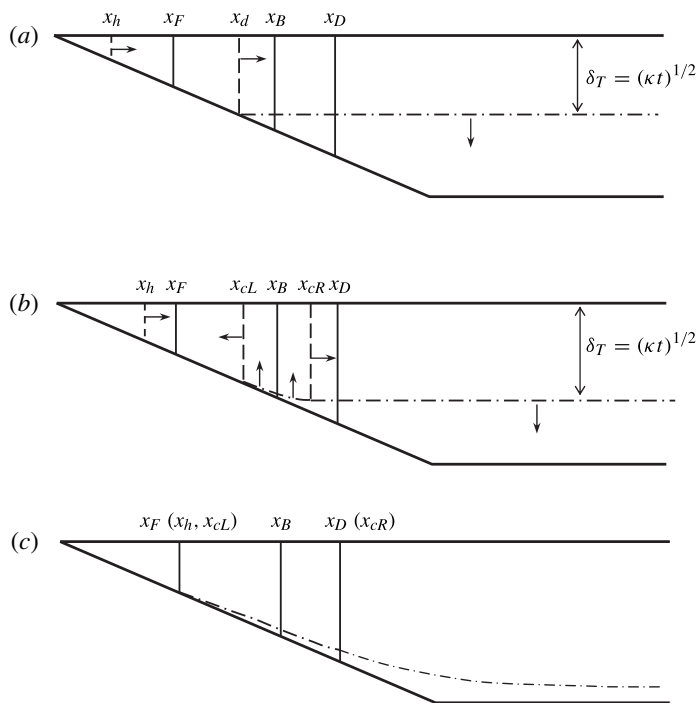


FIGURE 3. Schematic of the movement of the interfaces between different flow regions: (a) $t < t_B$; (b) $t_B < t < t_F$; (c) $t > t_F$. Here t_B denotes the time scale when the convection balance initially occurs, and t_F denotes the time scale when the right boundary of the conduction-dominated subregion meets the left boundary of the convection-dominated subregion. The dashed lines denotes the interfaces: x_d denotes the interface between the distinct and indistinct thermal boundary layer regions; x_h denotes the right boundary of the conduction-dominated subregion; x_{cL} and x_{cR} denote the left and right boundaries of the convection-dominated subregion, respectively; x_B denotes the position where the convection balance initially occurs; x_F denotes the position where the left boundary of the convection-dominated subregion and the right boundary of the conduction-dominated subregion meet each other; x_D denotes the position of the right boundary of the convection-dominated subregion at the quasi-steady state. The dash-dotted line denotes the boundary layer. The arrow indicates the direction of the movement.

flow reaches the quasi-steady state. Convection in the rest of the domain enhances with time. The expansion of the indistinct thermal boundary layer region stops when the interface x_d reaches the position x_B ; at the time ($t \sim t_B$) convection initially balances horizontal conduction at x_B . The conduction-dominated subregion continues to extend offshore and the horizontal temperature gradient in the region between x_h and x_B keeps increasing. The convection-dominated subregion begins to expand in both the onshore and offshore directions (the dashed lines x_{cL} and x_{cR} in figure 3b). The thermal boundary layer within the convection-dominated subregion (between x_{cL} and x_{cR}) shrinks with time. The thermal boundary layer in the region on the right side of x_{cR} still grows. When the interfaces x_h and x_{cL} eventually meet at the position x_F (at the corresponding time $t \sim t_F$), both the conduction-dominated and convection-dominated subregions stop developing. At that time ($t \sim t_F$), the right-hand interface of the convection-dominated subregion stops at the position x_D (figure 3c).

For $t > t_F$, the flow discharges into the region on the offshore side of x_D , which resembles an intrusion flow from the shore side of x_D . A detailed discussion on the flow intrusion can be found in Patterson & Imberger (1980). In this study, we mainly focus on the flow development at $t \leq t_F$.

In what follows, the detailed transient flow developments at different stages and in various subregions are described through scaling analysis.

3.2. Initiation of the flow

At time $t=0$, there is no flow and no heat transfer in the reservoir. At the early stage, both horizontal conduction and convection are negligible so that the heat input from the water surface is diffused vertically downwards to raise the water temperature. As a consequence, a thermal boundary layer starts to grow downwards underneath the water surface. A balance between the unsteady term and the diffusion term in the energy equation (2.4) yields a scale for the thickness of the thermal boundary layer (Mao *et al.* 2010)

$$\delta_T \sim (\kappa t)^{1/2}. \quad (3.1)$$

The temperature in this surface layer increases due to the heat input through the surface specified in (2.8). The temperature scale thus can be obtained as

$$T_s \sim H_0 \kappa^{-1/2} t^{1/2}. \quad (3.2)$$

Note that the scale T_s represents the temperature rise relative to the initial temperature T_0 . In this very early stage, the fluid is still at rest. This situation holds until the thermal boundary layer reaches the sloping bottom and becomes indistinct.

A comparison between the thickness of the thermal boundary layer (3.1) and the local water depth Ax results in the time scale for the thermal boundary layer to reach the sloping bottom,

$$t_d \sim A^2 x^2 \kappa^{-1}. \quad (3.3)$$

Clearly, with increasing offshore distance, it takes a longer time for the thermal boundary layer to reach the sloping bottom. This indicates that the indistinct thermal boundary layer region extends in the offshore direction. Within the indistinct thermal boundary layer region, the scale for the boundary layer thickness is the local water depth, i.e.

$$\delta_T \sim Ax. \quad (3.4)$$

At an arbitrary position x within the indistinct thermal boundary layer region, considering an infinitesimal water column of width dx , the energy balance in this water column gives

$$I_0 dx \sim \rho_0 C_p \delta_T dx \frac{dT_i}{dt}, \quad (3.5)$$

where T_i is the temperature of the water column. Substituting (3.4) into (3.5) yields the temperature scale within the indistinct thermal boundary layer region,

$$T_i \sim H_0 A^{-1} x^{-1} t. \quad (3.6)$$

Again, the scale T_i is not the temperature itself but the temperature rise relative to the initial temperature T_0 .

Equation (3.6) indicates that a horizontal temperature gradient establishes within the indistinct thermal boundary layer region, which results in a horizontal pressure

gradient that drives a flow away from the tip. As the bottom slope is assumed to be very small (usually $\ll 1$ in field situations), the vertical velocity component is negligible compared to the horizontal velocity component. A balance between the pressure term and the buoyancy term in the vertical momentum equation (2.3) yields a scale for the pressure p , by applying (3.4) and (3.6),

$$p \sim g\beta\rho_0 T_i \delta_T \sim g\beta\rho_0 H_0 t. \quad (3.7)$$

Mao *et al.* (2010) have shown that the viscous term in the horizontal momentum equation (2.2) is dominant in the indistinct thermal boundary layer region at the initial stage. This indistinct thermal boundary layer is shallow so that $\partial/\partial y \gg \partial/\partial x$. The balance in the horizontal momentum equation is thus between the viscous term and the buoyancy-induced pressure gradient, which yields a velocity scale of

$$u_n \sim g\beta H_0 A^2 v^{-1} x t \sim Ra A^2 \kappa^2 h^{-4} x t, \quad (3.8)$$

where Ra is the global Rayleigh number defined as

$$Ra = g\beta H_0 h^4 / \kappa^2 v. \quad (3.9)$$

Previous numerical and experimental studies (see e.g. Horsch *et al.* 1994; Bednarz, Lei & Patterson 2009b; Mao *et al.* 2010) have shown that the properties of the convective flow in a reservoir model such as the flow velocity vary along the horizontal direction. Adopting a fixed length scale in the scaling analysis would obscure the position-dependent flow features to be revealed. Thus, a variable horizontal length scale x is adopted in the present study. The same approach has been adopted in the previous scaling analyses of Mao *et al.* (2009, 2010) and has been proved to be appropriate by corresponding numerical simulations.

In the distinct thermal boundary layer region, the flow is passively driven by the pressure gradient induced in the indistinct thermal boundary layer region. Note that, in the distinct thermal boundary layer region, the boundary layer thickness and temperature scales are still governed by (3.1) and (3.2), respectively. The balance between the viscous term and the pressure gradient yields a velocity scale

$$u_f \sim g\beta H_0 \kappa v^{-1} x^{-1} t^2 \sim Ra \kappa^3 h^{-4} x^{-1} t^2. \quad (3.10)$$

It is worth noting that the velocity scale (3.10) is the same as that reported in Mao *et al.* (2010). Although the heat flux boundary conditions at the surface in these two studies have opposite signs (one for heating and the other for cooling), the same mechanism drives the flow in both cases, and thus the same velocity scale is expected. It is also worth noting that the horizontal flow considered here is in the opposite direction to that considered in Mao *et al.* (2010).

3.3. Extension of the indistinct thermal boundary layer region

The velocity scales given by (3.8) and (3.10) indicate that the velocity initially increases and then decreases along the x direction at an instantaneous time t (see figure 4). The peak velocity u_m occurs at the interface between the indistinct and distinct thermal boundary layer regions. By substituting (3.3) into (3.8) and (3.10), we found that the two velocity scales are identical at the interface, which represents the peak velocity at any given location x (achieved at time t_d),

$$u_m \sim Ra A^4 \kappa h^{-4} x^3. \quad (3.11)$$

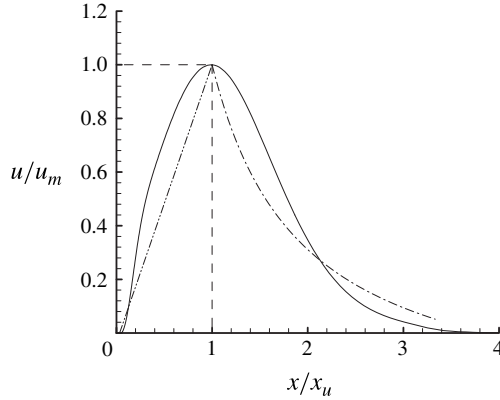


FIGURE 4. Sketch of the velocity profile along the x direction. Here u_m denotes the peak velocity and x_u denotes the corresponding location of u_m . Initially, with the passage of time, the peak velocity increases and its location moves in the offshore direction. The solid line denotes data at the water surface ($y = 0$) from numerical simulation, whereas the dash-dotted line denotes data from scaling analysis.

With the passage of time, the indistinct thermal boundary layer region extends in the offshore direction at a speed of u_i . The position where the peak velocity occurs ($x_u \sim (\kappa t)^{1/2}/A$) also moves at the velocity u_i in the offshore direction, which is given by

$$u_i \sim \delta_T A^{-1} t^{-1} \sim A^{-1} \kappa^{1/2} t^{-1/2}. \quad (3.12)$$

While heat is transferred into the thermal boundary layer through the surface heat flux, a horizontal temperature gradient is established after the thermal boundary layer reaches the sloping bottom. The heat entering the thermal boundary layer is thus conducted away by the horizontal temperature gradient. On the other hand, the horizontal temperature gradient induces a horizontal pressure gradient, which drives a flow in the offshore direction. Therefore, heat is also convected away by the flow induced by the horizontal pressure gradient.

3.4. Development of a conduction-dominated subregion

It is expected that the flow will achieve a steady or quasi-steady state after a certain time period, which is characterized by the steady velocity distribution in the whole reservoir. At the steady or quasi-steady state, the temperature gradient becomes steady in the whole reservoir; otherwise, the variation of temperature gradient would induce additional forces to accelerate or decelerate the flow. To maintain a steady temperature gradient across the entire reservoir, the temperature has to be constant or increase at the same rate everywhere in the reservoir. Since the reservoir model considered here is an enclosed domain with heat entering from the surface and no heat escaping from anywhere, it is expected that the temperature increases at the same rate but the temperature gradient remains steady in the entire reservoir at the quasi-steady state. Based on the above argument, the average temperature increase rate in the whole reservoir (considering that the flat-bottom region is much longer than the sloping-bottom region) can be calculated as

$$\frac{dT_{avg}}{dt} \sim H_0 h^{-1} \quad \text{or} \quad T_{avg} \sim H_0 t h^{-1}. \quad (3.13)$$

It is worth noting that the heat advected out of the domain is neglected in (3.13), which is appropriate for a sufficiently long domain. At a given location, when the convective flow reaches the quasi-steady state, part of the energy entering from the top surface is absorbed by the water and the rest is either conducted or convected away. In the indistinct thermal boundary layer region, the comparison between convection and horizontal conduction in (2.4) gives

$$\frac{\text{convection}}{\text{horizontal conduction}} \sim \frac{uTx^{-1}}{\kappa Tx^{-2}} \sim ux\kappa^{-1} \sim RaA^2\kappa h^{-4}x^2t. \tag{3.14}$$

Note that the velocity u in (3.14) is governed by scale (3.8).

From (3.14), it is found that conduction is dominant when $t_{com} < Ra^{-1}A^{-2}\kappa^{-1}h^4x^{-2}$, where t_{com} represents the time scale for heat transfer to switch from conduction-dominated to convection-dominated at a given x value. Within the indistinct thermal boundary layer region, for a particular location x_0 , the thermal boundary layer reaches the bottom at $t_{dx0} \sim A^2x_0^2\kappa^{-1}$. If $t_{dx0} < t_{com}$, the flow is still conduction-dominated, which gives $x_0 < Ra^{-1/4}A^{-1}h$. Thus, we can always find an $x_0 \sim Ra^{-1/4}A^{-1}h$ so that within the region $x < x_0$ the horizontal conduction term is larger than the convection term. In this region, the velocity stops increasing when horizontal conduction is strong enough to remove the excessive heat input from the surface that is not absorbed by the water. The energy balance in this region is thus written as

$$I_0x \sim \rho_0 C_p \kappa \left(-\frac{\partial T}{\partial x} \right) Ax + \frac{1}{2} \rho_0 C_p x Ax \frac{dT_{avg}}{dt}. \tag{3.15}$$

Substituting (3.13) into (3.15) gives

$$-\frac{\partial T}{\partial x} \sim H_0\kappa^{-1}A^{-1} \left(1 - \frac{Ax}{2h} \right). \tag{3.16}$$

Substituting (3.6) into (3.16) yields the time scale to reach the quasi-steady state,

$$t_h \sim \left(1 - \frac{Ax}{2h} \right) x^2\kappa^{-1}. \tag{3.17}$$

Equation (3.17) implies that the region where the quasi-steady state is achieved extends in the x direction with time. Horizontal conduction dominates in this region, which carries away the excessive heat that is not absorbed by the water. We shall refer to this region as the conduction-dominated subregion, which is a subregion in the indistinct thermal boundary layer region. It is worth noting that the internal energy change and the horizontal conduction were not accounted for in Mao *et al.* (2010), and the conduction-dominated and the indistinct thermal boundary layer regions were not distinguished in their study. As implied by (3.17), the conduction-dominated subregion expands in the offshore direction with time. Comparing (3.3) and (3.17) gives

$$\frac{t_h}{t_d} \sim \frac{1 - Ax/(2h)}{A^2} \sim A^{-2} - A^{-1}xh^{-1}. \tag{3.18}$$

We can then confirm that $t_h/t_d \gg 1$ because $A \ll 1$ and the maximum x value is $x \sim h/A$. Thus, the conduction-dominated subregion is always contained by the indistinct thermal boundary layer region.

3.5. Initiation of balance between convection and horizontal conduction

Equations (3.8) and (3.10) indicate that the velocity in the reservoir increases with time, resulting in an increase in convection. The convection term may eventually become comparable with the horizontal conduction term over a certain region. In such a region, the unabsorbed energy from the surface is removed from the layer by convection. It is shown above that the peak velocity occurs at the interface between the indistinct and distinct thermal boundary layer regions. At that point, local convection is maximum, which indicates that the energy balance should be initially achieved there, which gives

$$I_0 x \sim \rho_0 C_p u_m \delta_T T_c + \frac{1}{2} \rho_0 C_p x A x \frac{dT_{avg}}{dt}. \quad (3.19)$$

Note that in (3.19) the thickness of the thermal boundary layer and the velocity are governed by (3.4) and (3.11) respectively. The temperature scale T_c can be calculated from (2.8), giving

$$T_c \sim H_0 A x k^{-1}. \quad (3.20)$$

Substituting (3.4), (3.11), (3.13) and (3.20) into (3.19) gives

$$x^4 + 0.5 Ra^{-1} h^3 A^{-5} x - Ra^{-1} h^4 A^{-6} \sim 0. \quad (3.21)$$

From (3.21) we can obtain the position where the convection balance initially occurs (x_B). Although (3.21) can be solved analytically, it would be more convenient to yield the solution by asymptotic analysis or a numerical method. The asymptotic solution of x_B can be written as $x_B \sim [Ra^{-1/4} A^{-3/2} - (1/8) Ra^{-1/2} A^{-2} - (1/128) Ra^{-3/4} A^{-5/2}] h$. If the Rayleigh number is big enough so that $A x_B / (2h) \ll 1$, we can obtain

$$x_B \sim Ra^{-1/4} A^{-3/2} h. \quad (3.22)$$

The corresponding time scale t_B is obtained by substituting (3.22) into (3.3), which gives

$$t_B \sim Ra^{-1/2} k^{-1} A^{-1} h^2. \quad (3.23)$$

The variation of x_B with Ra is shown in figure 5. With increasing Ra , these solutions converge.

The thermal boundary layer stops growing once the energy balance is reached. This indicates that the indistinct thermal boundary layer region stops extending at the position x_B and the corresponding time t_B . Although the convection balance is achieved at $x \sim x_B$ and $t \sim t_B$, this does not mean that the development of flow within the indistinct thermal boundary layer region ($x < x_B$) stops. In fact, the region where the convection balance is achieved extends in both onshore and offshore directions from the initial position $x \sim x_B$ as demonstrated in §3.6. The indistinct thermal boundary layer region thus shrinks towards the tip region.

3.6. Expansion of the convection-dominated subregion

As shown in §3.4, the conduction-dominated subregion, which is within the indistinct thermal boundary layer region, extends from the tip region in the offshore direction. At the time $t \sim t_B$, the right boundary of the conduction-dominated subregion x_h satisfies $x_h < x_B$. Although the local energy balance is achieved at $x < x_h$ (conduction) and $x \sim x_B$ (convection), the horizontal temperature gradient in the region $x_h < x < x_B$

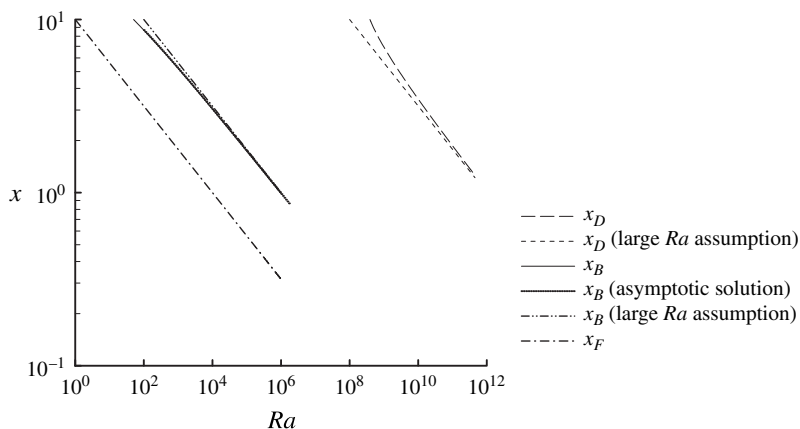


FIGURE 5. Variation of x_B , x_F and x_D with Ra (see the caption of figure 3 for the definitions of x_B , x_F and x_D). For x_B , the solid, dotted and dash-dotted-dotted lines denote the numerical solution of (3.21), the asymptotic solution and the approximate solution given by (3.22), respectively.

still increases, as neither convection nor horizontal conduction is strong enough to remove the excessive heat from that region. The horizontal pressure gradient also increases in this region, and so does the flow velocity. Thus, with the passage of time, convection outside the conduction-dominated subregion (i.e. for the region $x > x_h$) continuously increases until energy balance is achieved in this region.

For $t > t_B$, the conduction-dominated subregion continuously extends in the offshore direction with time, that is, x_h increases with time. As convection increases, convection in the region $x_h < x < x_B$ may eventually become strong enough to remove the unabsorbed heat from the region, which gives

$$I_0x \sim \rho_0 C_p u \delta_T T_c + \frac{1}{2} \rho_0 C_p x A x \frac{dT_{avg}}{dt}. \tag{3.24}$$

In the region $x_h < x < x_B$, the thermal boundary layer is indistinct. Thus the velocity in (3.24) is governed by (3.8). The thickness of the thermal boundary layer and the temperature scale T_c are governed by (3.4) and (3.20), respectively. The time scale at which the convection balance is achieved can then be obtained as

$$t_{cL} \sim Ra^{-1} h^4 A^{-4} \kappa^{-1} x^{-2} \left(1 - \frac{Ax}{2h} \right). \tag{3.25}$$

The corresponding position x_{cL} where the convection balance is achieved can be calculated from (3.25), which implies that x_{cL} moves backwards towards the tip region with time. Note that, at $t \sim t_B$, x_{cL} coincides with x_B . Thus, for $t > t_B$, the region where the convection balance is achieved extends from x_B towards the onshore region. We shall refer to the region as the convection-dominated subregion.

For the distinct thermal boundary layer region ($x > x_B$), convection also increases with time. Convection in this region may eventually become strong enough to remove the unabsorbed heat, which is also governed by (3.24). However, the thickness of the thermal boundary layer, the temperature and the velocity are now governed by (3.1),

(3.2) and (3.10), respectively. This energy balance yields the following time scale at which the convection balance is achieved:

$$t_{cR} \sim Ra^{-1/3} h^{4/3} \kappa^{-1} x^{2/3} \left(1 - \frac{Ax}{2h}\right)^{1/3}. \tag{3.26}$$

Once the convection balance is achieved, the thermal boundary layer stops growing. The corresponding position at which the convection balance is achieved, x_{cR} , can be calculated from (3.26), which implies that x_{cR} moves in the offshore direction with time. Note that, at $t \sim t_B$, x_c coincides with x_B . Thus, for $t > t_B$, the convection-dominated subregion also extends from x_B towards the offshore region.

The above analysis shows that for $t > t_B$ the convection-dominated subregion extends from x_B in both the onshore and offshore directions. The left and right boundaries of the convection-dominated subregion are x_{cL} and x_{cR} , respectively. For the region between x_h and x_{cL} , the horizontal temperature gradient still develops because no energy balance has been achieved. Thus, for the regions outside the conduction-dominated subregion ($x > x_h$), the horizontal pressure gradient still increases, and so does the velocity. This indicates that, even in the convection-dominated subregion, convection still keeps increasing after the convection balance is initially achieved. The thermal boundary layer in the convection-dominated subregion has to adjust in order to maintain the energy balance. This dynamic energy balance can still be described by (3.24). However, the velocity, temperature and thermal boundary layer thickness scales in (3.24) have to be re-evaluated.

In the convection-dominated subregion, the balance in the horizontal momentum equation is between the viscous term and the buoyancy-induced pressure gradient, which gives

$$\frac{p}{\rho_0 x} \sim v \frac{u}{\delta_T^2}. \tag{3.27}$$

It is worth noting that the pressure p in the above relation is still determined by the balance between the pressure gradient term and the buoyancy term in the vertical momentum equation (2.3), which leads to a scale for pressure similar to (3.7), that is, $p \sim g\beta\rho_0 T_c \delta_T$. However, in this case the thermal boundary layer thickness is unknown and is determined by neither (3.1) nor (3.4). Equation (3.27) can be rewritten as

$$u \sim g\beta H_0 v^{-1} t \delta_T^2 x^{-1} \sim Ra h^{-4} \kappa^2 t \delta_T^2 x^{-1}. \tag{3.28}$$

The temperature scale can be derived from the boundary condition (2.8), which gives

$$T_c \sim H_0 \delta_T \kappa^{-1}. \tag{3.29}$$

Substituting (3.28) and (3.29) into (3.24) gives

$$\delta_T \sim Ra^{-1/4} \kappa^{-1/4} t^{-1/4} x^{1/2} h \left(1 - \frac{Ax}{2h}\right)^{1/4}. \tag{3.30}$$

The velocity scale can then be obtained by substituting (3.30) into (3.28), yielding

$$u \sim Ra^{1/2} \kappa^{3/2} t^{1/2} h^{-2} \left(1 - \frac{Ax}{2h}\right)^{1/2}. \tag{3.31}$$

Equation (3.30) indicates that the thermal boundary layer thickness decreases with time. This means that the thickness of thermal boundary layer shrinks in the convection-dominated subregion while this region extends in both the onshore and offshore directions.

3.7. Quasi-steady state of convection- and conduction-dominated subregions

Equation (3.17) implies that the right boundary of the conduction-dominated subregion moves in the offshore direction with time. The analysis in § 3.6 shows that the convection-dominated subregion extends from x_B in both the onshore and offshore directions. In the region between the conduction-dominated and the convection-dominated subregions, the horizontal temperature gradient is still growing because neither horizontal conduction nor convection is sufficiently strong to carry away the unabsorbed heat. The horizontal temperature gradient stops growing only when the right boundary of the conduction-dominated subregion meets the left boundary of the convection-dominated subregion, i.e. $t_h \sim t_{cL}$, which gives

$$x_F \sim Ra^{-1/4} A^{-1} h, \tag{3.32}$$

and the corresponding time is

$$t_F \sim (1 - \frac{1}{2} Ra^{-1/4}) Ra^{-1/2} \kappa^{-1} A^{-2} h^2. \tag{3.33}$$

The variation of x_F with Ra is shown in figure 5. As $A \ll 1$, t_F is always larger than t_B .

At $t \sim t_F$, the conduction-dominated subregion stops extending in the offshore direction. At the quasi-steady state, the velocity scale for the conduction-dominated subregion can be obtained by substituting (3.17) into (3.8) as follows:

$$u \sim g\beta H_0 A^2 v^{-1} x t_h \sim Ra A^2 \kappa h^{-4} x^3 \left(1 - \frac{Ax}{2h}\right) \text{ for } x \lesssim x_F. \tag{3.34}$$

Once the horizontal temperature gradient stops increasing, the horizontal pressure gradient remains constant, and so does the velocity. Thus, the velocity in the convection-dominated subregion stops increasing, the region stops expanding, and the thickness of the thermal boundary layer stops shrinking. The left boundary of the convection-dominated subregion and the right boundary of the conduction-dominated subregion meet at $x \sim x_F$. The right boundary of the convection-dominated subregion stops at $t \sim t_F$, which can be obtained by substituting (3.33) into (3.26) as follows:

$$x^{2/3} \left(1 - \frac{Ax}{2h}\right)^{1/3} \sim \left(1 - \frac{1}{2} Ra^{-1/4}\right) Ra^{-1/6} A^{-2} h^{2/3}. \tag{3.35}$$

From (3.35) we can obtain the position of the right boundary of the convection-dominated subregion x_D . Equation (3.35) can be solved either analytically or numerically. For sufficiently high Rayleigh numbers $Ax_D/2h \ll 1$, we can obtain

$$x_D \sim Ra^{-1/4} A^{-3} h, \tag{3.36}$$

$$t_D \sim Ra^{-1/2} \kappa^{-1} A^{-2} h^2. \tag{3.37}$$

The variation of x_D with Ra is also shown in figure 5. Note that the solid line denotes the numerical solution of (3.35) whereas the dashed line denotes the approximate solution given by (3.36). At $t \sim t_F$, the thermal boundary layer in the convection-dominated subregion stops shrinking. The final scales for the thickness of the thermal boundary layer and the velocity can be obtained by substituting (3.33) into (3.30) and (3.31), respectively,

$$\delta_T \sim Ra^{-1/8} x^{1/2} A^{1/2} h^{1/2} \left(1 - \frac{1}{2} Ra^{-1/4}\right)^{-1/4} \left(1 - \frac{Ax}{2h}\right)^{1/4}, \tag{3.38}$$

$$u \sim Ra^{1/4} \kappa A^{-1} h^{-1} \left(1 - \frac{1}{2} Ra^{-1/4}\right)^{1/2} \left(1 - \frac{Ax}{2h}\right)^{1/2}. \tag{3.39}$$

The flow on the right side of the convection-dominated subregion may still develop after $t > t_F$. We shall refer to this region as the free-developing region. In this region, the flow is driven by the pressure gradient induced by the temperature gradient in the indistinct boundary layer region, which remains constant after $t > t_F$,

$$p_F \sim g\beta\rho_0 H_0 t_F. \tag{3.40}$$

The balance in the horizontal momentum equation is between the viscous term and the buoyancy-induced pressure gradient, which gives

$$\frac{p_F}{\rho_0 x} \sim \nu \frac{u}{\delta_T^2}. \tag{3.41}$$

The scale of the thermal boundary layer thickness in (3.41) is governed by (3.1). The velocity scale can be obtained by substituting (3.1) and (3.40) into (3.41), which yields

$$u \sim Ra^{1/2} \left(1 - \frac{1}{2} Ra^{-1/4}\right) A^{-2} h^{-2} \kappa^2 x^{-1} t. \tag{3.42}$$

The flow stops developing when the energy balance described by (3.24) is reached, which yields the time scale

$$t_s \sim Ra^{-1/4} \left(1 - \frac{1}{2} Ra^{-1/4}\right)^{-1/2} \left(1 - \frac{Ax}{2h}\right)^{1/2} Ax h \kappa^{-1}. \tag{3.43}$$

The final thermal boundary layer thickness and velocity scales at the quasi-steady state can then be obtained by substituting (3.43) into (3.1) and (3.42), respectively, which are exactly the same as (3.38) and (3.39).

3.8. Possible flow regimes

The time-dependent behaviour of the flow varies with the Rayleigh number. The possible developmental pathways of the flow at different Rayleigh numbers are summarized in table 1. If the Rayleigh number is sufficiently small ($Ra < 1$), the condition $h/A < x_F$ holds. In this case, horizontal conduction is always greater than convection. After sufficient time has elapsed, the thermal boundary layer attaches to the bottom in the whole reservoir. Subsequently, the horizontal temperature gradient continues to increase until it becomes significant enough to conduct away the heat input from the water surface and the quasi-steady state is achieved.

For medium Rayleigh numbers ($1 < Ra < Ra_i$), the condition $x_F < h/A < x_B$ holds. Note that Ra_i can be obtained by letting $x_B \sim h/A$, where x_B is determined by (3.21). The value of Ra_i is $O(A^{-2})$, which is ~ 50 if $A = 0.1$. After sufficient time has elapsed, the thermal boundary layer eventually attaches to the bottom in the whole reservoir, but the flow velocity keeps increasing. Horizontal conduction is dominant in the whole reservoir. Convection first becomes significant in the region with the maximum depth and the thermal boundary layer becomes distinct there again, which occurs at $t \sim t_B$. The indistinct thermal boundary layer region shrinks until $t \sim t_F$. At the quasi-steady state, the whole reservoir can be divided into two subregions, i.e. the conduction- and convection-dominated subregions. In the conduction-dominated subregion, the

velocity scale at the quasi-steady state is given by (3.34). In the convection-dominated subregion, the flow becomes steady at $t \sim t_F$; the corresponding thermal boundary layer thickness and velocity scales are described by (3.38) and (3.39), respectively.

For sufficiently high Rayleigh numbers ($Ra > Ra_i$), the condition $h/A > x_B$ holds. In this Rayleigh-number regime, the indistinct thermal boundary layer region does not occupy the whole reservoir during the developing stage and stops expanding when $t \sim t_B$ at $x \sim x_B$. The indistinct thermal boundary layer region then shrinks until $t \sim t_F$. At the quasi-steady state, the whole reservoir can be divided into the conduction-dominated and convection-dominated subregions.

4. Numerical procedures

As shown in figure 1, the computational model comprises two distinct regions: one with a sloped bottom and the other with a uniform water depth. This model is more realistic than the model of a triangular enclosure that has been adopted by Lei & Patterson (2006), Bednarz *et al.* (2008, 2009b) and Bednarz, Lei & Patterson (2009a,c). The slope inclination is fixed at $A = 0.1$. The lengths of the flat and the sloped parts are assumed to be equal, giving the total length of the model $L = 20h$. The non-dimensional governing equations can be expressed as

$$U_X + V_Y = 0, \quad (4.1)$$

$$U_\tau + UU_X + VU_Y = -(Pr Ra)P_X + Pr \nabla^2 U, \quad (4.2)$$

$$V_\tau + UV_X + VV_Y = -(Pr Ra)P_Y + Pr \nabla^2 V + (Pr Ra)\theta, \quad (4.3)$$

$$\theta_\tau + U\theta_X + V\theta_Y = \nabla^2 \theta, \quad (4.4)$$

with the non-dimensional surface heat flux condition,

$$\theta_Y = 1 \quad \text{at } Y = 0. \quad (4.5)$$

All the quantities in (4.1)–(4.5) have been normalized by the following scales: $X, Y \sim h$; $\tau \sim h^2 \kappa^{-1}$; $\theta \sim H_0 h \kappa^{-1}$; $U, V \sim \kappa h^{-1}$; $P \sim \rho_0 g \beta H_0 h \kappa^{-1}$. The Prandtl number Pr is defined as $Pr = \nu / \kappa$. As heat continuously enters the water body from the surface, the temperature of the water body keeps increasing. In this sense, there is no steady state with respect to the water temperature. However, a quasi-steady state may be reached in which temperature gradient and flow velocity become steady. At the quasi-steady state, temperature increases at the same rate everywhere, and thus the difference between the local temperature and the average temperature becomes steady.

The above non-dimensional governing equations along with the specified boundary and initial conditions are solved numerically using a finite-volume method. The second-order central difference scheme is applied for spatial derivatives in the governing equations. The second-order backward scheme is applied for time discretization in calculating the transient flow. The SIMPLEC method is adopted for pressure and velocity coupling. The non-staggered grid arrangement is applied and the interpolation of Rhie & Chow (1983) is used to get a good coupling between pressure and velocity. The detailed numerical procedures on discretization can be found in Ferziger & Perić (1999) and Yu *et al.* (2007). The validation of the present code for the simulation of natural convection in the reservoir model has been demonstrated in Yu *et al.* (2012a,b) and will not be repeated here.

The simulation is performed with a fixed Prandtl number of $Pr = 7$, which is relevant to water at room temperature. Before the final simulation, a mesh and

Mesh	260×20	320×40	480×60	640×80
Time step	2×10^{-6}	10^{-6}	0.7×10^{-6}	0.5×10^{-6}
U_{max}	64.52	64.13	63.90	63.78
Error (%)	1.16	0.55	0.19	—

TABLE 2. Effect of mesh size and time step on the predicted maximum velocity at the quasi-steady state.

time-step dependence test has been conducted using four different meshes, 260×20 , 320×40 , 480×60 and 640×80 for $Ra = 2.1 \times 10^5$, which is the highest among all the simulation cases. All the meshes are non-uniform, with higher grid density near all the boundaries. The time step is adjusted for different meshes so that the Courant–Friedrichs–Lewy (CFL) number remains approximately the same for different meshes. To avoid singularity at the tip, a very small tip region ($X = 0.16$) was cut off and an extra vertical wall was assumed there. The cutoff region accounts for less than 0.01% of the entire domain and thus has a negligible effect on the overall flow, except at the very beginning of the flow development.

Table 2 compares the predicted maximum horizontal velocity in the reservoir model obtained with all the meshes at the quasi-steady state. The error of the predicted maximum velocity with a chosen mesh related to that predicted with the finest mesh is also presented in the table. It is seen that the numerical error reduces and the predicted maximum horizontal velocity approaches a constant value with the increasing mesh resolution. It is expected that the variations of the solutions with the different meshes are even smaller at lower Rayleigh numbers. Based on these tests, mesh 2 is adopted for the present simulation and the corresponding time step is fixed at 10^{-6} .

5. Verification of the scaling analysis

The present study focuses on the transient behaviour of natural convection in the reservoir model induced by surface heating. Although the boundary condition considered in the present study is opposite to those in Lei & Patterson (2005) and Mao *et al.* (2010), which considered surface cooling, the underlying mechanism that drives the flow is the same except for the flow instability under the surface cooling conditions. In addition to the time-dependent behaviour of the flow, the present study has also revealed additional flow features that were not revealed in the previous scaling analyses of Lei & Patterson (2005) and Mao *et al.* (2010). Thus, this section will focus on verifying these newly discovered flow behaviours using the results of the numerical simulation. Flow visualizations showing the various stages of the transient flow development can be found in Mao *et al.* (2010) and Yu *et al.* (2012a), and are not repeated here for brevity. The simulations performed here cover a wide range of Rayleigh numbers (refer to table 3) to demonstrate all three possible flow development pathways. All the results presented in this section are normalized in the way described in § 4.

Note that the above-described scaling analysis is conducted based on the reservoir model with a triangular region connected with an infinite rectangular region. However, the present numerical simulation is performed in a reservoir model consisting of a triangular region and a finite rectangular region. For the former domain with a large and effectively infinite rectangular region, the average temperature increase rate can be

Flow regimes	Ra
$Ra < 1$	0.14, 0.014
$1 < Ra < Ra_i$	21
$Ra > Ra_i$	70, 2.1×10^3 , 7×10^3 , 2.1×10^4 , 7×10^4 , 2.1×10^5

TABLE 3. Rayleigh numbers adopted in the numerical validation.

obtained from (3.13). For the finite domain as shown in figure 1, the energy balance leads to

$$\frac{dT_{avg}}{dt} \sim \frac{4}{3}H_0h^{-1} \quad \text{or} \quad T_{avg} \sim \frac{4}{3}H_0th^{-1}. \quad (5.1)$$

Applying (5.1) to the scaling analysis in § 3 means that the prefactors of $(1 - Ax/(2h))$ and $(1 - Ra^{-1/4}/2)$ in the scaling relations (3.16)–(3.17), (3.25)–(3.26), (3.30)–(3.31), (3.33)–(3.35), (3.38)–(3.39) and (3.42)–(3.43) should be replaced by $(1 - 2Ax/(3h))$ and $(1 - 2Ra^{-1/4}/3)$, respectively, when comparing to our simulation results. For instance, the velocity scale at the quasi-steady state in the conduction-dominated subregion (see (3.34)) should be rewritten as

$$u \sim RaA^2\kappa h^{-4}x^3 \left(1 - \frac{2Ax}{3h}\right). \quad (5.2)$$

Our preliminary study shows that the new prefactors give a better prediction of the flow behaviour. Accordingly, the new prefactors will be used for the validation of the scaling relations.

5.1. Unsteady scales for the indistinct thermal boundary layer region

At the initial stage, the scaling analysis indicates that the instantaneous horizontal velocity increases and then decreases in the x direction ((3.8) and (3.10)). The peak velocity is located at the interface between the indistinct and distinct thermal boundary layer regions, which moves in the x direction with time. If the Rayleigh number is sufficiently low, the interface eventually reaches the end of the slope region at $\tau \sim 1$. At the same time, the thermal boundary layer in the whole flat region also reaches the bottom and becomes indistinct. As a consequence, the thermal boundary layer becomes indistinct over the entire flow domain, and the interface between the distinct and indistinct thermal boundary layer regions no longer exists. Since the peak velocity initially moves with the interface as shown in § 3.3, it remains at the end of the slope region after the disappearance of the distinct thermal boundary layer (i.e. for $\tau \gtrsim 1$).

Figure 6 shows the horizontal velocity profile along the water surface at different time for $Ra = 0.14$. For $\tau \lesssim 1$, the velocity first increases and then decreases in the offshore direction. The velocity is almost zero for X bigger than a certain value. The position of the peak velocity moves towards the offshore direction when $\tau \lesssim 1$, corresponding to the expansion of the indistinct thermal boundary layer region (3.12). The thermal boundary layer attaches to the bottom in the entire region at the time scale $\tau \sim 1$ (3.3). The position of the peak velocity then remains fixed with X of order h/A for $\tau \gtrsim 1$. These behaviours are consistent with the scaling analysis.

Mao *et al.* (2010) also proposed a velocity scale for the early stage of the flow development, which is the same as the present velocity scale (3.10). They considered this velocity scale as the sole velocity scale governing the flow in the early stage and reported that the velocity at any given time decreases monotonically with the

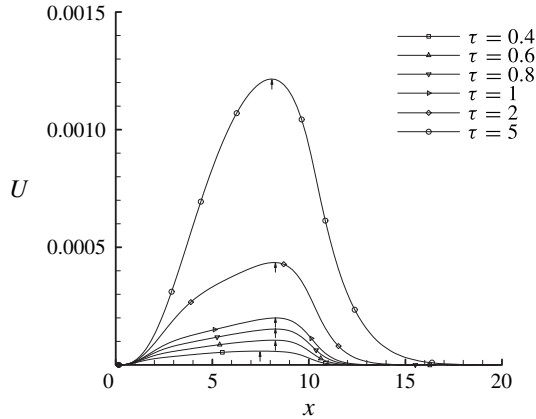


FIGURE 6. Horizontal velocity profiles along the water surface at different times for $Ra = 0.14$. The symbols on the plots are used to distinguish the curves at different times instead of representing the x locations where the U velocity is sampled. The arrows indicate the locations of the peak velocity.

offshore distance. However, both the present scaling analysis and numerical simulation indicate that the velocity initially increases and then decreases with the offshore distance. Therefore, the present study has provided a more comprehensive picture of the transient flow behaviour.

In the flow regime $Ra < 1$, the interface between the distinct and indistinct thermal boundary layer regions initially moves in the offshore direction with the extension of the indistinct thermal boundary layer region ($x_u \sim (\kappa t)^{1/2}/A$) until it reaches the end of the sloping region at $\tau \sim 1$. The interface disappears at $\tau \sim 1$ because the thermal boundary layer in the whole flat region also reaches the bottom and becomes indistinct as mentioned above. The location of the peak velocity then remains at the end of the sloping region for $\tau \gtrsim 1$. In the flow regime $Ra > 1$, the corresponding interface initially also moves in the offshore direction with the extension of the indistinct thermal boundary layer region ($x_u \sim (\kappa t)^{1/2}/A$) and then moves back towards the tip region with the shrinkage of the indistinct thermal boundary layer region (which can be derived from (3.25)). We record the position X_u of the peak U velocity along the water surface for the numerical simulation at different Rayleigh numbers and plot the data in figure 7(a). The curves for $Ra < 1$ indicate that the location of the peak velocity moves rapidly in the offshore direction when $\tau \lesssim 1$ and reaches around $X \sim 8.5$ at $\tau \sim 1$. For $\tau \gtrsim 1$, the location of the peak velocity stays around $X \sim O(10)$. The curves for $Ra > 1$ shows that X_u initially moves in the offshore direction and then retracts. All these results agree well with the scaling prediction. However, the velocity scale provided by Mao *et al.* (2010) indicated that the position of the peak U velocity only moves in the offshore direction, which cannot explain the retracting behaviour of the location of the peak velocity.

Note that there is a coarse stagger on the curves for $Ra < 1$ in figure 7(a). As mentioned in § 4, the computational meshes are non-uniform, with higher mesh density near all the boundaries. The distance between two neighbouring points around $X \sim O(10)$ is relatively large. The location of the peak velocity may drift between two neighbouring points due to numerical errors, which may in turn cause the obvious staggers on the curves. These staggers may be avoided by using a finer

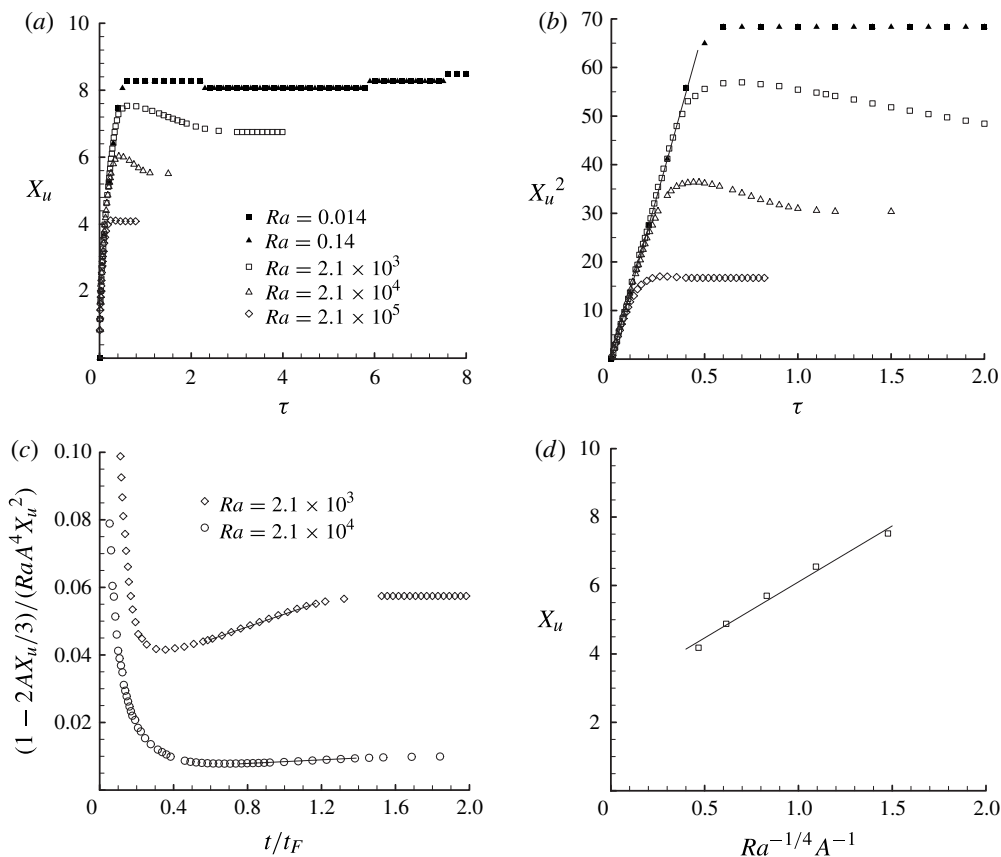


FIGURE 7. The transient behaviour of the position of the peak U velocity along the surface: (a) time history of the position; (b) validation of the scale for $t < t_B$; (c) validation of the scale for $t_B < t < t_F$; (d) validation of the scale for the quasi-steady state ($Ra > 1$). The Rayleigh numbers are indicated in the panels. The symbols denote the numerical results and the solid line is a linear fit in (b–d).

mesh in the horizontal direction. However, this would require a significant increase in computational time. Given that the present numerical results are sufficiently accurate to capture the major flow features, the present mesh is adopted, although its resolution in the region around $X \sim O(10)$ is relatively low.

The time scale for the thermal boundary layer to reach the sloping bottom is governed by the scale (3.3). The dimensionless form of the scale can be rewritten as $\tau_d \sim A^2 X^2$. As mentioned previously, the peak flow velocity occurs at the interface between the indistinct and distinct thermal boundary layer regions. Accordingly, X_u^2 linearly increases with time at the initial stage for all the Rayleigh numbers as shown in figure 7(b). The curves deviate from the linear relationship for $t > t_B$ (curves for $Ra > 1$) or $t > h^2/\kappa$ (curves for $Ra < 1$).

The time scale for the shrinkage of the indistinct thermal boundary layer is governed by the scale (3.25). The dimensionless form of the scale can be rewritten as $\tau_{cL} \sim (1 - 2AX/3)/(RaA^4X^2)$ if the new prefactor $(1 - 2Ax/(3h))$ determined by (5.1) is applied. Note that the position of the peak velocity along the surface X_u is located at the interface between the indistinct and distinct thermal boundary layer

regions, which moves in the $-x$ direction with the shrinkage of the indistinct thermal boundary layer region as shown in figure 7(a). Figure 7(c) shows the time history of $(1 - 2AX_u/3)/(RaA^4X_u^2)$. The time is rescaled by t_F (refer to the scale (3.33)). As shown in figure 7(c), the function $(1 - 2AX_u/3)/(RaA^4X_u^2)$ increases linearly with time over the time period of $0.4 < t/t_F < 1.5$ for $Ra = 2.1 \times 10^3$ and 2.1×10^4 . This is consistent with the behaviour of the scale (3.25) in the retracting stage ($t_B < t < t_F$). It is also seen in figure 7(c) that the curves for $Ra = 2.1 \times 10^3$ and 2.1×10^4 do not collapse onto each other. This is because the magnitude of τ_{cL} in the scale (3.25) is both Ra - and position-dependent, and the scale (3.25) is only valid when $t_B < t < t_F$. Therefore, it is difficult to rescale the plots to make the curves for the different Rayleigh numbers collapse onto each other. Nevertheless, figure 7(c) shows a linear relationship around $t/t_F \sim O(1)$ for the different Rayleigh numbers, which is consistent with the prediction of the scale (3.25).

At the final quasi-steady state, the location of the interface X_u remains at x_F (3.32) for $Ra > 1$. Figure 7(d) shows the locations of X_u at the quasi-steady state obtained from the simulation for different Rayleigh numbers against the scaling of $x_F \sim Ra^{-1/4}A^{-1}h$. It demonstrates an approximately linear correlation between the numerical data and the scaling prediction, which further validates the present scaling analysis. However, it may be argued that the numerical data shown in figure 7(d) exhibit a power-law relationship with the scaling prediction. As described in the above scaling analysis, at the quasi-steady state, the peak velocity is located at the interface between the conduction-dominated and convection-dominated subregions. The scaling analysis is based on the assumption that there is a sharp transition between the conduction- and convection-dominated subregions. However, a transitional region, in which both conduction and convection are important, exists in reality. This modifies the energy balances ((3.19) and (3.24)) and causes the deviation between the numerical simulation and scaling prediction.

5.2. Unsteady scales for the conduction-dominated subregion

The scaling analysis suggests that the conduction-dominated subregion extends in the offshore direction with time. As described in the preceding scaling analysis, the conduction-dominated subregion is always within the indistinct thermal boundary layer region. For very low Rayleigh numbers ($Ra < 1$), the conduction-dominated subregion keeps expanding even after the thermal boundary layer has encompassed the whole sloping region. The final quasi-steady state in the entire reservoir occurs at the time scale $\tau \sim A^{-2}/2 = 50$ (estimated from (3.17)).

It is worth mentioning that Mao *et al.* (2010) obtained the same time scale $t_d \sim A^2x^2/\kappa$ for the thermal boundary layer to reach the sloping bottom. They also considered t_d as the time scale for the flow in the indistinct thermal boundary layer region to reach the quasi-steady state, i.e. the flow reaches the quasi-steady state once the thermal boundary layer reaches the sloping bottom. Therefore, there is no distinction between the indistinct thermal boundary layer region and the conduction-dominated subregion in their analysis. The present scaling analysis reveals that the developments of the flow and the horizontal temperature gradient in the indistinct thermal boundary layer region continue after the thermal boundary layer has reached the sloping bottom. The conduction-dominated subregion develops within the indistinct thermal boundary layer region until $t \sim t_h$. The developing time for the flow to reach the quasi-steady state is thus much longer than that predicted by Mao *et al.* (2010). The numerical results indeed support our scaling analysis, as will be shown later.

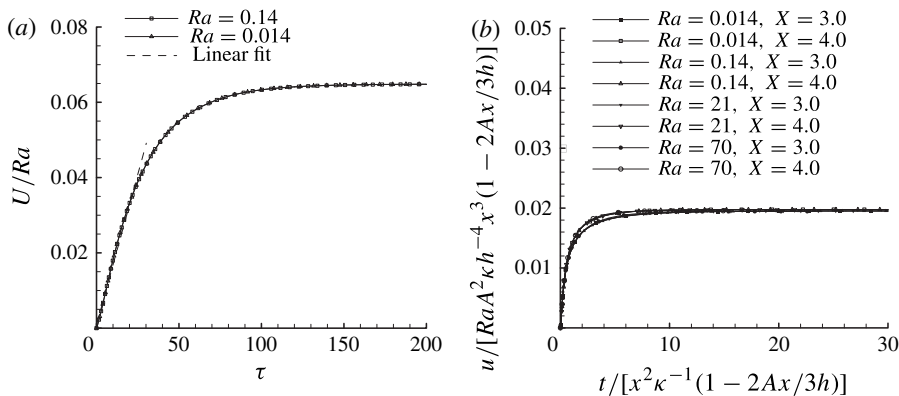


FIGURE 8. Time histories of (a) the peak U velocity along the water surface and (b) the u velocity at two fixed locations on the water surface. The Rayleigh numbers are indicated in the panels. The velocity and time are normalized as shown.

Figure 6 shows that the horizontal velocity keeps increasing when $\tau \gg \sim 1$, which suggests that the horizontal temperature gradient is still increasing after the thermal boundary layer reaches the bottom in the entire reservoir. The development of the flow stops only if horizontal conduction is significantly strong to remove the excessive heat entering from the surface.

We also record the time histories of the peak horizontal velocity along the water surface for $Ra = 0.014$ and 0.14 in figure 8(a). Here the peak velocity presented in figure 8(a) is further normalized by Ra . The scaling analysis indicates that the peak velocity is governed by (3.11). When $\tau \gtrsim 1$, the thermal boundary layer has reached the bottom in the entire reservoir. The velocity is governed by scale (3.8). As the peak velocity is located at $x \sim h/A$ for $\tau \gtrsim 1$, the peak velocity scale becomes $u_m \sim RaAk^2h^{-3}t$. Thus, the peak velocity is a linear function of time for $\tau \gtrsim 1$. This situation holds until $\tau \sim A^{-2}/2 = 50$ (see figure 8a), i.e. the time scale for the quasi-steady state in the sloping region as given by the scale (3.17). As expected, the calculated velocities for the two different Ra values collapse onto one curve, as shown in figure 8(a).

The above scaling analysis shows that, in the indistinct thermal boundary layer region, the velocity is a linear function of both the position and time. The flow within this region reaches the quasi-steady state at $t \sim t_h$, which is position-dependent, as indicated by (3.17). At the quasi-steady state, the velocity in the conduction-dominated subregion is governed by (3.34). To validate the velocity scale, the time histories of the horizontal surface velocity at different Rayleigh numbers from the simulations are plotted with the position as a parameter in figure 8(b). The velocity and time in the figure are normalized by the scales $u \sim RaA^2\kappa h^{-4}x^3(1-2Ax/(3h))$ (scale (3.34) with the new prefactor) and $t_h \sim (1-2Ax/(3h))x^2\kappa^{-1}$ (scale (3.17) with the new prefactor), respectively. The scaling analysis shows that the conduction-dominated subregion is confined in the tip region $x < x_F$. Thus, we choose relatively small values of x to ensure that the positions where the velocities are recorded are well within this region.

As shown in figure 8(b), all the curves collapse after the velocity and the time from the simulations are normalized by the corresponding scales. Figure 8(b) also shows that, at the initial stage, the velocity increases approximately linearly with time. The development of the velocity stops at $t/[x^2\kappa^{-1}(1-2Ax/(3h))] \sim O(1)$. These flow behaviours agree well with the prediction of the scaling analysis.

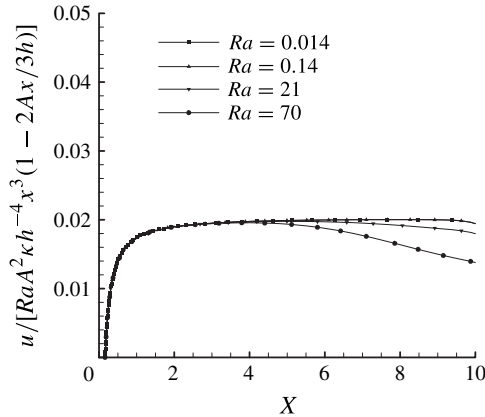


FIGURE 9. Profiles of the U velocity along the water surface from the simulation.

Figure 9 shows the normalized velocity profiles along the x direction by using the modified scale (5.2), i.e. with the new prefactor $(1 - 2Ax/(3h))$. The curves for $Ra = 0.014$ and 0.14 collapse onto each other, indicating that conduction is dominant in the entire slope region at these low Rayleigh numbers. It is noted in figure 9 that the curves for $Ra = 21$ and 70 deviate from those for $Ra < 1$ when X is beyond a certain value. As indicated by the scaling analysis, the region far away from the tip region becomes convection-dominated for $Ra > 1$. The velocity in the convection-dominated subregion does not follow the velocity scale of (5.2) and thus deviates from those for $Ra < 1$. The position of the deviating point moves towards the tip region with increasing Ra because the conduction-dominated subregion becomes smaller at larger Ra (refer to the variation of x_F with Ra in figure 5). It is worth noting that using the prefactor $(1 - Ax/(2h))$, which is appropriate for a large and effectively infinite rectangular domain, does not match the expected asymptote, but the new prefactor $(1 - 2Ax/(3h))$ derived for the finite domain does. This observation further confirms that the change in the internal energy of the water body has to be taken into account when considering the energy balance. All these results further verify the present scaling analysis.

5.3. Unsteady scales for the convection-dominated subregion

For high Rayleigh numbers ($Ra > 1$), convection becomes dominant in the region far from the tip region. The scaling analysis shows that the horizontal pressure gradient still increases after the balance between convection and horizontal conduction is initially achieved at $x \sim x_B$. Thus, the horizontal velocity also increases and convection enhances. The convection-dominated subregion expands in both the onshore and offshore directions, while the indistinct thermal boundary layer region shrinks. The shrinkage of the indistinct thermal boundary layer region has been demonstrated by the time history of the location of the peak surface horizontal velocity X_u , as shown in figure 7(a). To further show the expansion of the convection-dominated subregion in the onshore direction, the time evolution of the isotherms for $Ra = 2.1 \times 10^5$ are shown in figure 10. At the very early time $t = 0.005$, the isotherms are horizontal and parallel in most regions of the reservoir except for the tip region. The isotherms are curled in the tip region in order to satisfy the no-flux conduction there, indicating

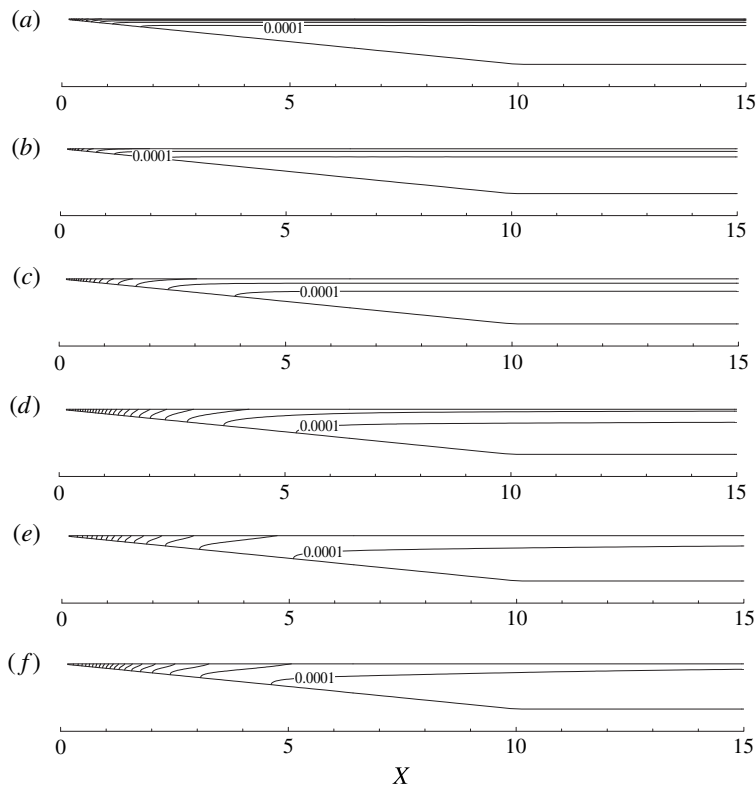


FIGURE 10. Isotherms in the reservoir at different time instants for $Ra = 2.1 \times 10^5$. Isotherms at: (a) $t = 0.005$ with an interval of 0.02; (b) $t = 0.01$ with an interval of 0.05; (c) $t = 0.05$ with an interval of 0.1; (d) $t = 0.25$ with an interval of 0.2; (e) $t = 0.5$ with an interval of 0.5; (f) $t = 1$ with an interval of 0.5.

that the thermal boundary layer attaches to the bottom and an indistinct thermal boundary layer region forms. The contour lines with a very small non-zero value of 10^{-4} are marked in figure 10(b–f). It is shown that the 10^{-4} contour line first moves in the offshore direction and then retracts in the onshore direction. If this contour line is regarded as an indicator of the interface between the distinct and indistinct thermal boundary layer regions, the expansion and retraction of the indistinct thermal boundary layer region is then indicated by the positions of the 10^{-4} contour lines. The retraction of the 10^{-4} contour line also indicates a decrease in temperature there.

The above scaling analysis reveals that the dominant mode of heat transfer varies with time and position. To validate this, the horizontal heat transfer rates by conduction and convection are calculated from the simulation results. The total horizontal heat transfer rate, including the contributions of both conduction and convection, is averaged over the local water depth and defined in a dimensionless form as

$$H(X) = \frac{1}{|Y_b|} \int_{Y_b}^0 (U\theta^* - \theta_x^*) dY, \quad (5.3)$$

where θ^* is the spatial variation of the temperature (spatial deviation from the average temperature in the reservoir) and Y_b is the corresponding Y coordinate of the bottom at a given horizontal position X .

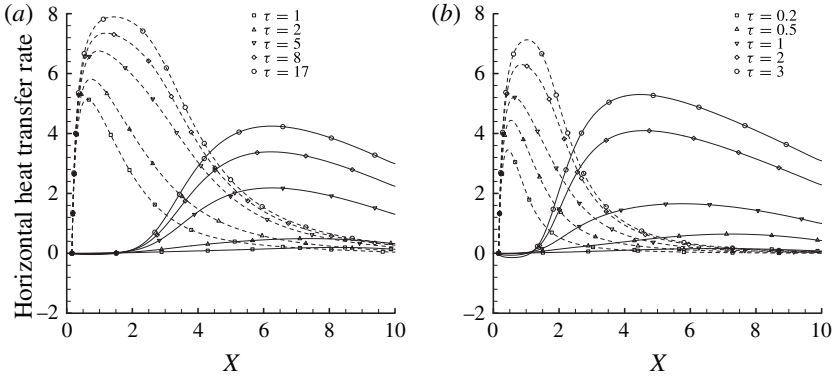


FIGURE 11. Profiles of the horizontal convection (solid lines) and conduction (dashed lines) heat transfer rates averaged over the local water depth at different time instants for (a) $Ra = 2.1 \times 10^3$ and (b) $Ra = 2.1 \times 10^4$.

It is worth mentioning that (5.3) has been successfully used in the previous studies (Lei & Patterson 2005; Mao *et al.* 2009, 2010) to characterize the quasi-steady flow behaviours. The present study will further show the transient behaviours of flow properties. Figure 11 shows the profiles of the horizontal heat transfer rates averaged over the local water depth calculated at different times for $Ra = 2.1 \times 10^3$ and 2.1×10^4 , respectively, which also compares the relative intensities of convection and conduction along the x direction. The intersection of the convection and conduction curves at a particular time indicates that convection and conduction are equally important there. Clearly, this figure shows that the intersection moves towards the tip region with time, which indicates the expansion of the convection-dominated subregion towards the onshore direction. All the transient flow results presented above provide strong evidence to support the present scaling analysis.

Further, the time history of the x coordinate of the intersection X_i obtained from the numerical simulation for $Ra = 2.1 \times 10^3$ and 2.1×10^4 is recorded. The scaling analysis shows that the time scale for the balance between convection and vertical conduction is governed by (3.25). It is expected that there is a linear relationship between $(1 - 2AX_i/3)/(RaA^4X_i^2)$ and t/t_F during the developing stage of the convection-dominated subregion, i.e. for $t_B < t < t_F$, which is confirmed in figure 12(a). The two curves for $Ra = 2.1 \times 10^3$ and 2.1×10^4 do not collapse onto each other. The reason for this is the same as that for X_u , as explained in figure 7(c).

At the quasi-steady state, the location of the interface X_i stays at x_F (3.32) if $Ra > 1$. The locations of X_i at the quasi-steady state obtained from the simulation for different Rayleigh numbers are plotted against the scaling of $x_F \sim Ra^{-1/4}A^{-1}h$ in figure 12(b). The excellent linear correlation between the numerical data and the scaling prediction demonstrates that the location of X_i at the quasi-steady state is well predicted by the scaling analysis.

The scaling analysis indicates that the flow in the convection-dominated subregion reaches the quasi-steady state at the same time. To validate this time scale, the surface velocities at different locations for $Ra = 2.1 \times 10^5$ are shown in figure 13(a). All the locations selected are within the convection-dominated subregion and also within the sloping-bottom region to ensure the validity of the scale. Indeed, all the curves in this figure indicate that the flow in the whole convection-dominated subregion reaches the

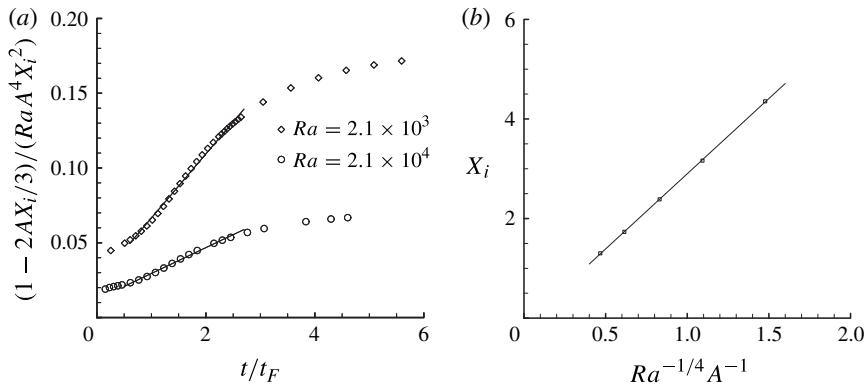


FIGURE 12. (a) Time history of the x coordinate of the intersection of the horizontal convection and conduction heat transfer curves X_i from the numerical simulation for $Ra = 2.1 \times 10^3$ and 2.1×10^4 . (b) The locations of X_i at the quasi-steady state from the simulation versus the scaling predictions at various Rayleigh numbers ($Ra > 1$). The symbols denote the numerical results whereas the solid lines are linear fits.

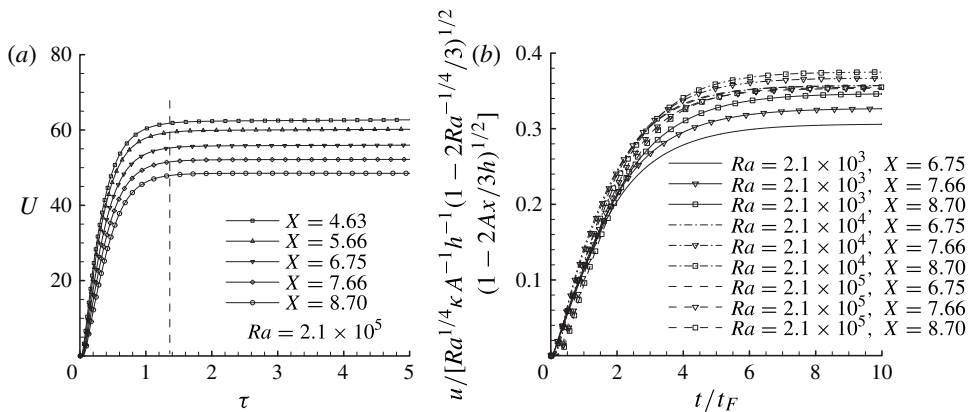


FIGURE 13. Time history of (a) the U velocity and (b) the renormalized u velocity at fixed locations on the water surface. The locations and the Rayleigh numbers are indicated in the panels. The velocity and time are normalized as shown.

quasi-steady state at the same time. Simulations for other Rayleigh numbers also show the same result. The previous numerical simulations reported in Yu *et al.* (2012b) also support this result.

It is worth noting that Mao *et al.* (2010) reported a time scale $t_c \sim x^{2/3}Ra^{-1/3}h^{4/3}\kappa^{-1}$ for the flow in the convection-dominated subregion to reach the quasi-steady state, which suggests that the steady-state time depends on the location. Clearly the present scaling analysis and numerical simulation do not support their prediction (refer to figure 13a).

To validate the velocity scale for the convection-dominated subregion, the time histories of the horizontal surface velocity at different Rayleigh numbers from the simulations are plotted with the position as a parameter in figure 13(b). The

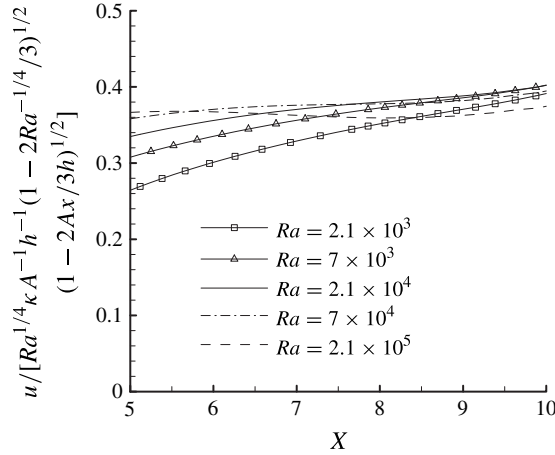


FIGURE 14. Profiles of the U velocity along the water surface from the numerical simulation normalized by the relevant scale for the convection-dominated subregion.

velocity and time in the figure are normalized by the scales $u \sim Ra^{1/4}\kappa A^{-1}h^{-1} \times (1 - 2Ra^{-1/4}/3)^{1/2}(1 - 2Ax/(3h))^{1/2}$ ((3.39) with the new prefactor) and $t_F \sim (1 - 2Ra^{-1/4}/3)Ra^{-1/2}\kappa^{-1}A^{-2}h^2$ ((3.33) with the new prefactor), respectively. The values of x are chosen carefully to ensure that they are within the convection-dominated subregion. As shown in figure 13(b), with the normalization, all the curves become fairly close to each other despite some scattering, suggesting that the scaling gives a reasonable prediction for the transient flow velocity. It is also seen in figure 13(b) that the development of the flow velocity at all the Rayleigh numbers and locations stops at $t/t_F \sim 5$, again confirming the validity of the scale for the steady-state time.

Figure 14 shows the profiles of the U velocity along the water surface at the quasi-steady state. The velocity is normalized by the velocity scale for the convection-dominated subregion at the quasi-steady state (3.39). It is expected that the normalized velocity in the convection-dominated subregion at different Ra collapses onto a horizontal straight line because this velocity scale embodies the Rayleigh number and position dependences. As can be seen in figure 14, the normalized velocity profiles approximately converge to a horizontal line for X beyond a certain value (this value is Ra -dependent and corresponds to the convection-dominated subregion). Although the curve for $Ra = 2.1 \times 10^5$ deviates slightly from the other curves for $X > 9$, the deviation is considered negligibly small for the purpose of demonstrating the scaling. It is also worth emphasizing that the unscaled values of U in figures 13(b) and 14 vary by a factor of 4, but the rescaling reduces the variability to less than 30% of the mean value. Thus, the simulation results generally support the scaling analysis.

6. Conclusions

In the present study, a scaling analysis coupled with numerical simulations has been performed to investigate the transient behaviour of natural convection in a reservoir model. An improved scaling analysis, which takes into account the internal energy change and the effect of horizontal conduction, has been carried out to

reveal new and more detailed features of the transient flow development than the previously reported analyses (e.g. Lei & Patterson 2005; Mao *et al.* 2009). Position- and time-dependent scales have been established to quantify the flow properties. Depending on the Rayleigh number, three possible flow regimes corresponding to three different flow development pathways towards the final quasi-steady state (as shown in table 1) can be classified, i.e. the low-Rayleigh-number regime with $Ra < 1$, the medium-Rayleigh-number regime with $1 < Ra < Ra_i$, and the high-Rayleigh-number regime with $Ra > Ra_i$. These Rayleigh-number-based criteria are equivalent to the following criteria based on the length of the sloping region: $h/A < x_F$, $x_F < h/A < x_B$ and $h/A > x_B$, respectively.

The present scaling analysis reveals that horizontal conduction plays an important role in the transient flow behaviour. Initially, the thermal boundary layer reaches the sloping bottom in the tip region, and the unequal heat gain associated with the changing water depth results in a horizontal temperature gradient. This temperature gradient in turn establishes a horizontal pressure gradient that drives a flow towards the offshore direction. The indistinct thermal boundary layer region expands towards the offshore direction. In the meantime, the horizontal conduction eventually becomes strong enough near the tip region so that it removes the excessive heat input from the surface. The flow in this horizontal conduction-dominated subregion becomes quasi-steady. The horizontal conduction-dominated subregion also expands in the offshore direction with time. Outside the conduction-dominated subregion, the flow velocity keeps increasing.

The schematic of the development pathways towards the final quasi-steady state has been summarized in figure 2. At time $t \sim t_B$, convection at $x \sim x_B$ becomes strong enough to balance the heat input from the surface. The expansion of the indistinct thermal boundary layer region stops here and a convection-dominated subregion appears. Between the horizontal conduction-dominated subregion and the convection-dominated subregion, the horizontal temperature gradient still increases, the horizontal velocity driven by the horizontal pressure gradient also increases, and so does convection. As the horizontal temperature gradient increases, the conduction-dominated subregion continues to expand in the offshore direction at $t > t_B$. In the meantime, the shore-side extent of the convection-dominated subregion moves towards the tip region, resulting in the shrinkage of the indistinct thermal boundary layer region. Within the convection-dominated subregion, the initially indistinct thermal boundary layer detaches from the sloping bottom and shrinks due to the increase of convection. The shrinkage of the thermal boundary layer stops at $t \sim t_F$ and the indistinct thermal boundary region finally coincides with the conduction-dominated subregion. The above-described transient flow behaviour is fully confirmed by the numerical simulations.

Built on the previous studies of Lei & Patterson (2005) and Mao *et al.* (2010), a more thorough understanding of the near-shore natural convection flow driven by constant heat flux has been achieved. Fundamental differences between the present study and the previous ones (Lei & Patterson 2005; Mao *et al.* 2010) are that the present study: (a) takes into account the change of the internal energy contained by the water body when considering the energy balance; (b) accounts for the effect of horizontal conduction; and (c) develops a comprehensive scaling for transient convection leading to the quasi-steady state. The scaling analysis conducted in the present study also explains the contradictions between the scaling analysis of Mao *et al.* (2010) and the numerical simulation of Yu *et al.* (2012a).

The present scaling results are readily applicable to predicting the surface heat flux-induced flow in field situations, in which the value of the Rayleigh number is

much larger than Ra_i . In this case, the developments of the distinct and indistinct thermal boundary layer regions, the conduction-dominated and convection-dominated subregions, can be quantified by the present study. More specifically, the order of magnitude of the flow velocity at any given time and a given location and the time scales for the transitions between the different flow states, as well as the length scales of the different flow subregions, can be readily predicted. However, the present study only considers a constant heating flux at the water surface. In real field situations, the thermal forcing varies, depending on the time of day and the weather conditions. The combined effect of the variation of the thermal forcing and the inertia of the flow may result in more complex flow behaviour. Also, turbulent convection may develop at the much larger Ra expected in field situations. Therefore, further understanding of these types of flow relevant to field conditions entails future investigations.

REFERENCES

- ADAMS, E. E. & WELLS, S. A. 1984 Field measurements on side arms of Lake Anna Va. *J. Hydraul. Engng* **110**, 773–793.
- BEDNARZ, T., LEI, C. & PATTERSON, J. C. 2008 An experimental study of unsteady natural convection in a reservoir model cooled from the water surface. *Exp. Therm. Fluid Sci.* **32**, 844–856.
- BEDNARZ, T., LEI, C. & PATTERSON, J. C. 2009a A numerical study of unsteady natural convection induced by iso-flux surface cooling in a reservoir model. *Intl J. Heat Mass Transfer* **52**, 56–66.
- BEDNARZ, T., LEI, C. & PATTERSON, J. C. 2009b An experiment study of unsteady natural convection in a reservoir model subject to periodic thermal forcing using combined PIV and PIT techniques. *Exp. Fluids* **47**, 107–117.
- BEDNARZ, T., LEI, C. & PATTERSON, J. C. 2009c Unsteady natural convection induced by diurnal temperature changes in a reservoir with slowly varying bottom topography. *Intl J. Therm. Sci.* **48**, 1932–1942.
- FARROW, D. E. 2004 Periodically forced natural convection over slowly varying topography. *J. Fluid Mech.* **508**, 1–21.
- FARROW, D. E. & PATTERSON, J. C. 1994 The daytime circulation and temperature pattern in a reservoir sidearm. *Intl J. Heat Mass Transfer* **37**, 1957–1968.
- FERZIGER, J. H. & PERIĆ, M. 1999 *Computational Methods for Fluid Dynamics*, 2nd edn. Springer.
- HORSCH, G. M. & STEFAN, H. G. 1988 Convective circulation in littoral water due to surface cooling. *Limnol. Oceanogr.* **33**, 1068–1083.
- HORSCH, G. M., STEFAN, H. G. & GAVALI, S. 1994 Numerical simulation of cooling-induced convective currents on a littoral slope. *Intl J. Numer. Meth. Fluids* **19**, 105–134.
- LEI, C. & PATTERSON, J. C. 2002a Natural convection in a reservoir sidearm subject to solar radiation: a two-dimensional simulation. *Numer. Heat Transfer A* **42**, 13–32.
- LEI, C. & PATTERSON, J. C. 2002b Unsteady natural convection in a triangular enclosure induced by absorption of radiation. *J. Fluid Mech.* **460**, 181–209.
- LEI, C. & PATTERSON, J. C. 2003 A direct stability analysis of a radiation-induced natural convection boundary layer in a shallow wedge. *J. Fluid Mech.* **480**, 161–184.
- LEI, C. & PATTERSON, J. C. 2005 Unsteady natural convection in a triangular enclosure induced by surface cooling. *Intl J. Heat Fluid Flow* **26**, 307–321.
- LEI, C. & PATTERSON, J. C. 2006 Natural convection induced by diurnal heating and cooling in a reservoir with slowly varying topography. *JSME Intl J. Ser. B* **49**, 605–615.
- MAO, Y., LEI, C. & PATTERSON, J. C. 2009 Unsteady natural convection in a triangular enclosure induced by absorption of radiation – a revisit by improved scaling analysis. *J. Fluid Mech.* **622**, 75–102.
- MAO, Y., LEI, C. & PATTERSON, J. C. 2010 Unsteady near-shore natural convection induced by surface cooling. *J. Fluid Mech.* **642**, 213–233.

- MONISMITH, S. G. 2007 Hydrodynamics of coral reefs. *Annu. Rev. Fluid Mech.* **39**, 37–55.
- MONISMITH, S. G., GENIN, A., REIDENBACH, M. A., YAHEL, G. & KOSEFF, J. R. 2006 Thermally driven exchanges between a coral reef and the adjoining ocean. *J. Phys. Oceanogr.* **36**, 1332–1347.
- MONISMITH, S. G., IMBERGER, J. & MORISON, M. L. 1990 Convective motions in the sidearm of a small reservoir. *Limnol. Oceanogr.* **35**, 1676–1702.
- PATTERSON, J. & IMBERGER, J. 1980 Unsteady natural convection in a rectangular cavity. *J. Fluid Mech.* **100**, 65–86.
- PHILLIPS, O. M. 1970 On flows induced by diffusion in a stably stratified fluid. *Deep-Sea Res.* **17**, 435–443.
- RHIE, C. M. & CHOW, W. L. 1983 Numerical study of the turbulent flow past an airfoil with trailing edge separation. *AAIA J.* **21**, 1525–1532.
- STURMAN, J. J., OLDHAM, C. E. & IVEY, G. N. 1999 Steady convective exchange flows down slopes. *Aquat. Sci.* **61**, 260–278.
- WUNSCH, C. 1970 On oceanic boundary mixing. *Deep-Sea Res.* **17**, 293–301.
- YU, P., LEE, T. S., ZENG, Y. & LOW, H. T. 2007 A numerical method for flows in porous and open domains coupled at the interface by stress jump. *Intl J. Numer. Meth. Fluids* **53**, 1755–1775.
- YU, P., LEI, C. & PATTERSON, J. C. 2012a Transient behaviour of natural convection in a reservoir model induced by surface heating. *J. Therm. Sci. Technol.* **7**, 211–226.
- YU, P., LEI, C. & PATTERSON, J. C. 2012b A numerical simulation of transient near-shore natural convection induced by ramped iso-flux cooling. *Intl J. Heat Fluid Flow* **38**, 107–117.